Nanoscale

Accepted Manuscript

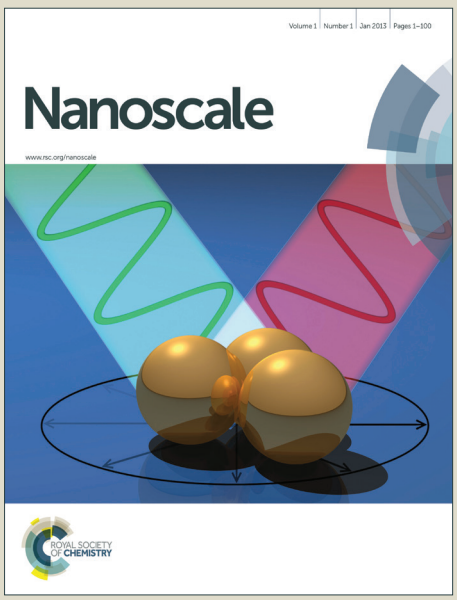

ROYAL SOCIETY OF CHEMISTRY

www.rsc.org/nanoscale

Cite this: DOI: 10.1039/c0xx00000x

www.rsc.org/xxxxxx

ARTICLE TYPE

Magnetic/NIR-responsive drug carrier, multicolor cell imaging, and enhanced photothermo-therapy of gold capped magnetite-fluorescent carbon hybrid nanoparticles

Hui Wang,[a] Guixin Cao,[b] Zheng Gai,[b] Kunlun Hong,[b] Probal Banerjee[a] and Shuiqin Zhou [a]

Received (in XXX, XXX) Xth XXXXXXXXX 20XX, Accepted Xth XXXXXXXXX 20XX
DOI: 10.1039/b000000x

The paper reports a type of multifunctional hybrid nanoparticles (NPs) composed of gold nanocrystals coated on and/or embedded in the magnetite-fluorescent porous carbon core-shell NP template (Fe_3O_4@PC-CDs-Au) for biomedical applications, including magnetic/NIR-responsive drug release, multicolor cell imaging, and enhanced photothermal therapy. The synthesis of the Fe_3O_4@PC-CDs-Au NPs involves the first preparation of the core-shell template NPs with magnetite nanocrystals clustered in core and fluorescent carbon dots (CDs) embedded in the porous carbon shell, followed by an in-situ reduction of silver ions (Ag^+) loaded in the porous carbon shell and a subsequent replacement of Ag NPs with Au NPs through a galvanic replacement reaction using $HAuCl_4$ as precursor. The Fe_3O_4@PC-CDs-Au NPs can enter into the intracellular region and light up the mouse melanoma B16F10 cells in multicolor modal. The porous carbon shell anchored with hydrophilic hydroxyl/carboxyl groups endow the Fe_3O_4@PC-CDs-Au NPs with an excellent stability in aqueous phase and a high loading capacity (719 mg g^{-1}) for the anti-cancer drug of doxorubicin (DOX). The superparamagnetic Fe_3O_4@PC-CDs-Au NPs with a saturation magnetization of 23.26 emu/g produce a localized heat under an alternating magnetic field, which triggers the release of the loaded drug. The combined photothermal effects of Au nanocrystals and CDs on/in the carbon shell cannot only regulate the release rate of the loaded drug, but also efficiently kill tumor cells under the NIR irradiation. Benefited from their excellent optical properties, magnetic field and NIR light responsive drug release, and enhanced photothermal effect, such nanostructured Fe_3O_4@PC-CDs-Au hybrid NPs provide a great promise for the simultaneous imaging diagnostics and high efficacy therapy.

1. Introduction

Carbon-based nanomaterials have gained significant momentum in recent years because of their wide applications in biomedical areas such as cell imaging, drug carrier and photothermal therapy.[1-5] Owing to their large specific surface area, porous structure, non-specific binding site and biocompatibility, carbon-based nanomaterials have been explored for highly effective and economical transmembrane drug delivery carriers that can release drug molecules inside the tumor cells for effective chemotherapy.[6-12] However, the actual accumulation and lack of controlled drug release of the carbon-based carriers at the specific tumor site remain big problems. The exogenous site targeting and responsive drug release strategy using an external stimulus such as magnetic field or near infrared (NIR) light should be a promising solution to overcome the current problems. Moreover, the external stimulus strategy could be more suitable for in vivo applications because they do not need change the specific physical or chemical properties (pH, temperature) of the environmental medium, which may cause severe side-effects to normal cells and tissues.[13-16] For example, the passive accumulation of magnetic-functionalized carbon-based drug carrier could be a convenient way for remotely enhancing the drug accumulation at the tumor site when an external magnetic field is applied.[17-19] Furthermore, magnetic-functionalized carbon-based drug carrier can trigger the release of loaded drug by a simple exposure to an appropriate alternating magnetic field benefited from the hyperthermia of magnetic NPs in alternating magnetic field.[20-24] On the other hand, NIR light has been widely used as an external stimulus to control the drug release due to its low energy absorption, deep penetration and minimal side effects for human tissue and organs.[25,26] A NIR-responsive drug carrier brings a new opportunity to release the loaded drug at a desired area and time by applying NIR light on the tumor site, which can obviously improve the therapeutic efficacy in cancer treatment while minimizing side effects.[27-32] Carbon-based drug carriers, functionalized with inorganic NPs that can efficiently convert NIR photons to heat, have demonstrated NIR-responsive drug release.[33-38] Meanwhile, the elevated temperatures of the NIR-responsive drug carrier under NIR irradiation could synergistically kill the tumor cells and thus improve the therapeutic efficacy.[39] Since traditional chemotherapeutic drugs bring severe side-effects such as liver, kidney, and cardio toxicity, the enhanced therapeutic efficacy of the combined chemo- and photothermo- therapy using the NIR-responsive drug carriers make it possible to lower down the drug doses, which is expected to minimize systemic side-effects of chemotherapeutic agents.[40-42]

The purpose of this manuscript is to develop a kind of multifunctional carbon-based drug carriers that can realize both the magnetic targeted drug accumulation and the magnetic/NIR dual responsive drug release. Considering the high NIR photothermal conversion ability and biocompatibility of gold (Au) NPs,[43-46] we design a hybrid nanostructure to integrate the superparamagnetic iron oxide (Fe_3O_4) and Au nanocrystals into a porous carbon NP embedded with fluorescent carbon dots (CDs). Specifically, the preparation of the designed Fe_3O_4@PC-CDs-Au hybrid NPs involves the first synthesis of Fe_3O_4@PC-CDs core-shell template NPs with Fe_3O_4 nanocrystals clustered in core and fluorescent CDs embedded in the porous carbon shell, followed by an in-situ reduction of silver ions (Ag^+) adsorbed on the porous carbon shell and a subsequent replacement of Ag with Au NPs through a galvanic replacement reaction using $HAuCl_4$ as precursor. As illustrated in Fig. 1, such prepared hybrid NPs can combine the functions from each component into a single nano-object to realize a multifunctional nanoplatform. The porous carbon shell with hydrophilic surface hydroxyl and carboxyl groups of the hybrid NPs is designed to load drug molecules and provide high stability of the NPs in aqueous solutions. While the magnetite nanocrystals in the core are designed to provide magnetic site-targeting and magnetic induced heating controllable drug release, the Au NPs are designed for the NIR photothermal therapy and NIR triggered drug release. Meanwhile, the CDs embedded in the carbon shell can exhibit excellent optical properties, including the bright multicolor fluorescent emissions and NIR photothermal effect. As expected, the resultant Fe_3O_4@PC-CDs-Au hybrid NPs with size about 100 nm cannot only enter the intracellular region and light up the mouse melanoma B16F10 cells in multicolor modal, but also demonstrate a high loading capacity (719 mg g^{-1}) for the anti-cancer drug doxorubicin and magnetic/NIR dual responsive drug release under the external stimuli including an alternating magnetic field and NIR light. The addition of Au nanocrystals onto the Fe_3O_4@PC-CDs template NPs further enhance the NIR photothermal effect of the hybrid NPs, therefore significantly improve the therapeutic efficacy compared to the chemo-therapy alone.

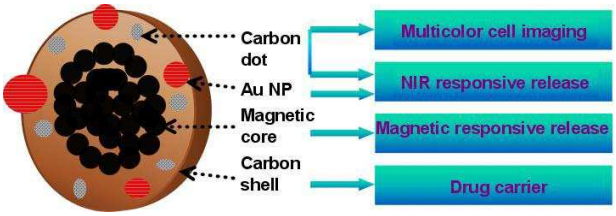

Fig. 1. Schematic illustration of the multifunctional Fe_3O_4@PC-CDs-Au hybrid NPs. The porous carbon shell embedded with fluorescent CDs cannot only provide fluorescent cell imaging ability, but also provide high drug loading capacity and NIR-responsive drug release. The addition of gold nanocrystals can further enhance the NIR photothermal effect to kill more tumor cells and thus significantly improve the therapeutic efficacy. Furthermore, the superparamagnetic iron oxide nanocrystals in the core can produce a localized heating under an alternating magnetic field to trigger the release of loaded drug molecules.

2. Experimental Section

2.1 Materials

All chemicals were purchased from Aldrich. Ferrocene ($Fe(C_5H_5)_2$, ≥98%), hydrogen peroxide (H_2O_2, 30%), acetone (C_3H_6O) and ethanol (C_2H_6O), silver nitrate ($AgNO_3$), sodium borohydride ($NaBH_4$), L-ascorbic acid, chloroauric acid ($HAuCl_4$) were used as received without further purification. The water used in all experiments was of Millipore Milli-Q grade.

2.2 Synthesis of Fe_3O_4@PC-CDs-Au hybrid NPs

The Fe_3O_4@PC-CDs core-shell template NPs were firstly synthesized using a one-pot solvothermal method.[47] Briefly, 0.10 g ferrocene dissolved in 30 mL acetone was intensely sonicated for 30 min at 25 °C, followed by a slow addition of 2.5 mL of 30 % H_2O_2 solution. The precursor solution was then vigorously stirred for 30 min and transferred to a 50.0 mL Teflon-lined stainless autoclave. After sealing it, the autoclave was heated to and maintained at 200 °C to allow the reaction going for 48 h. The naturally cooled reaction products were then intensely sonicated for 15 min and magnetically separated using a 0.30 T rare earth magnet (5 cm×5 cm×2.5 cm). The obtained black solid product was then washed with acetone three times and dried at room temperature in a vacuum oven. Then, Ag NPs were in-situ synthesized on the template NPs by the first adsorption of silver ions into the carbon shell, followed by the reduction of silver ions under the assistance of sodium borohydride. Briefly, 1 mL aqueous solution (0.1 mol/L) of silver nitrate and 5 mL suspension (500 mg/L) of Fe_3O_4@PC-CDs template NPs were transferred to a 20 mL vial. After a vigorous stirring for 15 min, 5 mL aqueous solution (0.01 mol/L) of sodium borohydride was added into the mixture and the final solution volume was added to 20 mL by using distilled water. This precursor solution was heated to and maintained at a temperature of 30 °C under a magnetic stirring for 15 min to ensure the reduction of silver ions to Ag metal. The resultant Fe_3O_4@PC-CDs-Ag NPs were then magnetized for 10 min by a magnet (0.30 T) and the supernatant was discarded. The precipitates were washed five times with distilled water to remove free Ag nanocrystals under an external magnetic field. Finally, the Fe_3O_4@PC-CDs-Ag NPs were dried and collected for the synthesis of Fe_3O_4@PC-CDs-Au NPs using the galvanic replacement reaction.[48,49] Briefly, the Fe_3O_4@PC-CDs-Ag NPs were redispersed into 10 mL water and stirred in an ice water bath for 30 min, 0.5 mL solution of $HAuCl_4$ (0.1 mol/L) was then added dropwise. The immediate color change revealed the galvanic replacement reaction between Ag and Au(III). The solution was stirred for another 20 min until the color was stable. After that, a solution of L-ascorbic acid (100 mM, 0.4 mL) was added dropwisely to allow the seed-mediated growth of Au nanocrystals. The reaction was continued for 15 min. The final Fe_3O_4@PC-CDs-Au NPs from the reaction medium were magnetized for 10 min by a 0.30 T magnet and the supernatant was discarded. The precipitates were redispersed into 10 mL distilled water by intensive sonication for 30 min and then separated again by the magnet for 10 min. This magnetic separation-ultrasound redispersion washing process was repeated for five times with distilled water at 25 °C to remove the free Au nanocrystals. Finally, the Fe_3O_4@PC-CDs-Au NPs were dried at room temperature.

2.3 DOX drug loading and release of the Fe_3O_4@PC-CDs-Au hybrid NPs

The drug loading was performed by adding Fe_3O_4@PC-CDs-Au NPs (1 mg) into 10 mL phosphate buffered saline (PBS) solution (0.005 M, pH = 7.4) containing 1 mg DOX under a magnetic stirring at 37 °C for 48 h. The mixture was then separated by a 0.30 T magnet. In order to remove unloaded DOX, the precipitate was redispersed in 10 mL PBS solution of pH = 7.4 and further purified by repeated separation and washing until the separated solution is clear. All the washed and separated solutions were collected and combined. The amount of unloaded free-DOX molecules in the combined solution was quantified by a UV-Vis spectrophotometer at 480 nm. The drug loading content of the Fe_3O_4@PC-CDs-Au NPs was calculated by $[(M_0 - M_t)/M_N] \times 100\%$, where M_0 and M_t are the mass of DOX in the initial

solution and separated solution, respectively. M_N is the mass of Fe_3O_4@PC-CDs-Au NPs used in the loading process.

The in vitro release profile of DOX from the Fe_3O_4@PC-CDs-Au NPs was evaluated by the dialysis method. The DOX-loaded Fe_3O_4@PC-CDs-Au NPs were redispersed in 10 mL PBS solution (0.005 M, pH = 7.4). Two dialysis bags filled with 2.5 mL DOX-loaded Fe_3O_4@PC-CDs-Au NPs with a known concentration were immersed in 50 mL 0.005 M PBS solutions of pH = 7.4 at 37 ^{o} C without or with NIR irradiation of 1.5 W/cm^{2}output power at certain releasing time intervals. The magnetic-responsive release experiments of DOX-loaded Fe_3O_4@PC-CDs-Au NPs at 37 °C were performed by applying an alternating magnetic field at certain time intervals using a magnetic generator (100 V, 0.8 A, 50 Hz). The released DOX molecules outside the dialysis bags were sampled at defined time periods and assayed by UV-Vis spectrometry at 480 nm. Cumulative release is expressed as the total percentage of drug released through the dialysis membrane over time.

2.4 Internalization of Fe_3O_4@PC-CDs-Au NPs into mouse melanoma cells B16F10

Round glass cover slips were placed in wells of a 24-well plate and treated with 0.1% poly-L-lysine in 100 mM PBS solution for 40 min. Following the treatment, the solution was aspirated and the wells were washed with PBS 3 times each. Next, B16F10 cells (2×10^4 cell/well) were plated on the glass coverslips at 80% confluence in DMEM containing 10% FBS and 1% penicillin-streptomycin. After 24 h, 500 µL of Fe_3O_4@PC-CDs-Au NPs (0.1 mg/mL) in serum-free DMEM were added to the marked wells. In a control well, 500 µL of serum-free DMEM was added. The plate was incubated at 37 °C for 2 h. The medium was then aspirated and fresh serum-free DMEM was added to each well. Finally, the coverslips with cells were removed from the wells and mounted onto slides for confocal microscopy study.

2.5 In vitro cytotoxicity of DOX-free and DOX-loaded Fe_3O_4@PC-CDs-Au NPs with or without NIR irradiation

B16F10 cells were cultured in the 96 wells microplate in 100 µL medium containing about 2,000 cells seeded into each wells. After an overnight incubation for attaching, remove the medium and add another 100 µL medium containing DOX-free and DOX-loaded Fe_3O_4@PC-CDs-Au NPs to make the final extract concentration of 100 µg/mL, 75 µg/mL, 50 µg/mL and 25 µg/mL, respectively. Wells used the normal medium without samples were used as control. For photothermal treatments, the cells were irradiated with 1.5 W/cm^2 NIR light for 5 min. After incubated for 24 h, 10 µL of 3-(4,5-dimethyl-2-thiazolyl)-2,5-diphenyltetrazolium bromide (MTT) solution (5 mg/mL in PBS) was added into the wells. The wells were further incubated in a humidified environment of 5 % $CO_2$and 37 °C for 2 h. The medium were removed after 2 h and 100 µL of DMSO solution is added. The plates were gently agitated until the formazan precipitate was dissolved, followed by measurement of OD value by spectrophotometer at 570 nm and 690 nm.

2.6 Characterizations

Transmission electron microscopy (TEM) images were taken on an FEI TECNAI transmission electron microscope at an accelerating voltage of 120 kV. High-resolution transmission electron microscopy (HRTEM) images were obtained by JEM 2100 (JEOL with an acceleration voltage of 200 kV. Approximately 10 µL of the diluted multifunctional hybrid NPs suspension was air-dried on a carbon-coated copper grid for the TEM measurements. Energy-dispersive X-ray (EDX) analysis was obtained with an EDAX detector installed on the same HRTEM. The powder X-ray diffraction (XRD) patterns were collected on a Japan Rigaku D/MAX-γA X-ray diffractometer equipped with Cu Kα radiation (λ = 1.542 Å) over the 2θ range of 20–70°. The FT-IR spectra of the solid hybrid NPs were recorded with a Nicolet Instrument Co. MAGNA-IR 750 Fourier transform infrared spectrometer. The UV-vis absorption spectra of the hybrid NPs dispersed in water were obtained on a Thermo Electron Co. Helios β UV-vis Spectrometer. The photoluminescence (PL) spectra of the aqueous dispersions of the hybrid NPs were obtained on a JOBIN YVON Co. FluoroMax®-3 Spectrofluorometer equipped with a Hamamatsu R928P photomultiplier tube, calibrated photodiode for excitation reference correction from 200 to 980 nm, and an integration time of 1 s. Nitrogen adsorption–desorption measurements were carried out on a Micromeritics ASAP 2020 instrument. The photothermal experiments for the hybrid NPs dispersed in water or buffer solutions were conducted using a Philips infrared reflector lamp with a power density of 1.5 W cm^{-2} and a filter to block the ultraviolet-visible light. The magnetic thermal experiments on the hybrid NPs were conducted using a magnetic generator (100 V, 0.8 A, 50 Hz). A superconducting quantum interference device (SQUID) magnetometer (Quantum Design MPMS XL-7) was used to measure the magnetic properties of as-prepared samples. The B16F10 cells incorporated with hybrid NPs were imaged using a confocal laser scanning microscopy (LEICA TCS SP2 AOBS^{TM}) equipped with a HC PL APO CS 20×0.7 DRY len.

3. Results and discussion

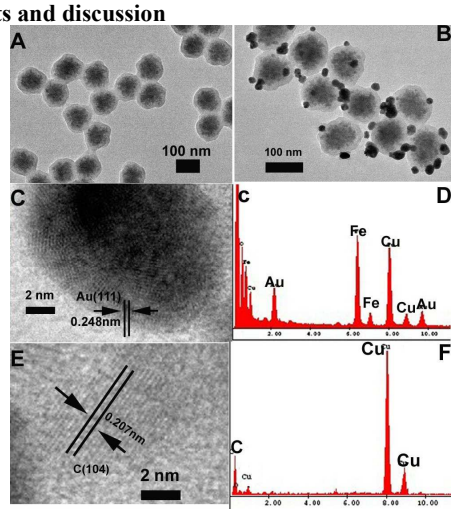

Fig. 2. (A) TEM image of Fe_3O_4@PC-CDs NPs. (B) TEM image of Fe_3O_4@PC-CDs-Au NPs. (C and D) HRTEM image and EDAX of the single gold nanocrystal and single Fe_3O_4@PC-CDs-Au NP. (E and F) HRTEM image and EDAX of the carbon dot embedded in the carbon shell.

Our strategy to prepare the multifunctional Fe_3O_4@PC-CDs-Au NPs involves the first synthesis of Fe_3O_4@PC-CDs core-shell structured template NPs, followed by loading and in-situ reduction of Ag^+ ions to embedded the Ag nanocrystals in the porous carbon shell of Fe_3O_4@PC-CDs NPs under the assistance of $NaBH_4$ and a final replacement of Ag with Au nanocrystals using a galvanic replacement reaction between the $HAuCl_4$ and the pre-formed Ag nanocrystals (see schematic illustration in Supporting Information Fig. S1). The one-pot solvothermal synthetic mechanism of the Fe_3O_4@PC-CDs NPs from the decomposition and oxidation of ferrocene with H_2O_2 at 200 ºC in acetone has been described in our previous work.[47] Briefly, the ferrocene quickly decomposes to iron and cyclopentadiene. The rupture of C-H bonds in the cyclopenta-1,3-diene leads to many small carbon-based free radicals, which can form relatively large carbon-based fragments or NPs with disordered (amorphous carbon) or ordered (CD) structure under the high temperature and high pressure from the gasification of solvent acetone.

Meanwhile, the O_2 decomposed from H_2O_2 oxidizes the Fe atoms to form Fe^{2+} and iron oxide. The Fe^{2+} in turn catalyze the decomposition of H_2O_2 to form highly reactive free radicals (e.g., HO· and HOO·), which can speed up the oxidation of Fe to form iron oxide nanocrystals and rapidly react with carbon fragment free radicals to form –OH and –COOH groups. The iron oxide nanocrystals can aggregate into larger secondary cluster. Then the carbon-based fragments or NPs in amorphous (porous) or ordered (crystalline CD) structure with surface –OH/–COOH groups can be adsorbed onto the surface of the iron oxide nanocrystal clusters. The carbon atoms deposited on the surface of iron oxide NPs are highly mobile under the reaction conditions, resulting in a coated layer with small CDs randomly trapped in the amorphous carbon carrying –OH/–COOH groups on their pore surface. Fig. 2A shows the typical TEM image of the obtained Fe_3O_4@PC-CDs template NPs, which shows a clear core–shell structure with the dark-contrasted Fe_3O_4 nanocrystals mainly dispersed in the carbon matrix in the core region but nearly no presence in the outmost light-contrasted carbon layer. The NPs are in a spherical morphology with an average size about 110 nm in diameter. The XRD pattern of the obtained Fe_3O_4@PC-CDs NPs (Fig. S2) with reflections indexed as 220, 311, 400, 422, 511, and 440 confirms the presence of magnetite nanocrystals with a size of about 9.2 nm calculated from the Debye–Scherrer formula.[50] In addition, the FT-IR spectrum of the Fe_3O_4@PC-CDs NPs exhibits a broad absorption at about 3386 cm^{-1} and a strong absorption at about 1708 cm^{-1} (Fig. S3). The broad peak at about 3386 cm^{-1} can be attributed to the -OH group and the absorption at ~1708 cm^{-1} can be assigned to the characteristic C=O stretching mode of the carboxylic acid groups conjugated with condensed aromatic carbons.[51,52] Clearly, the IR spectrum confirms the presence of the –COOH and/or –OH groups in the Fe_3O_4@PC-CDs NPs. While the porous structure of the amorphous carbon matrix allows the diffusion of precursor Ag^+ ions, the carboxylate groups on the pore surface can electrostatically immobilize the Ag^+ ions and thus enable the successful loading of Ag^+ ions into the inner pores as well as onto the exterior surface. After loaded with Ag^+ ions, the template Fe_3O_4@PC-CDs NPs can be easily converted to Fe_3O_4@PC-CDs-Ag hybrid NPs with Ag nanocrystals embedded in the porous carbon matrix as well as anchored on the exterior surface of the carbon shell (See Fig. S4A) via an in-situ reduction of Ag^+ ions under the assistance of sodium borohydride. The immobilization of Ag nanocrystals shifted the –OH and –COOH bands slightly in the IR spectrum of the Fe_3O_4@PC-CDs-Ag hybrid NPs compared to that of the Fe_3O_4@PC-CDs NPs due to the binding of these groups with Ag metal (Fig. S3). The energy dispersive analysis of X-rays (EDAX) of the single Fe_3O_4@PC-CDs-Ag NP (Fig. S4B) also confirms the successful deposition of the Ag nanoscrystals in the porous carbon matrix or on the exterior surface of the template Fe_3O_4@PC-CDs NPs. To synthesize the Fe_3O_4@PC-CDs-Au NPs, the Ag nanocrystals in the carbon shell were replaced with Au nanocrystals through a galvanic replacement reaction between Ag nanocsytals and $HAuCl_4$. Fig. 2B shows the TEM image of the resulted Fe_3O_4@PC-CDs-Au NPs, which shows that Au nanocrystals are trapped in or attached on the porous carbon shell. It should be mentioned that the observed structure of the hybrid NPs should be real. Although our TEM sample was prepared from the regular air-drying of the aqueous dispersion of Fe_3O_4@PC-CDs-Au NPs, we believe that only those Au NPs stably immobilized via the –OH/-COOH groups will still stay inside or on the surface of the template NPs and there should be very limited number of free Au NPs staying in the water after the five repeated cycles of magnetic separation-ultrasound redispersion process. Compared to the TEM image of the corresponding Fe_3O_4@PC-CDs-Ag template NPs (Fig. S4A), the Fe_3O_4@PC-CDs-Au NPs show more large metal nanocrystals but less small metal nanocrystals. This morphology evolution is reasonable. It has been observed that solid Ag nanowires can evolve to hollow Au nanotubes in the course of the galvanic replacement reaction, because such a reaction in aqueous solution involves multiple steps, including the reconstruction of the Au nanocrystals.[53] The EDAX (Fig. 1D) of the single Fe_3O_4@PC-CDs-Au NP laid on the TEM grid reveals the presence of Fe, Au, O, C, and Cu elements. In comparison with the presence of Fe, Ag, O, C, and Cu elements in the EDAX profile of the Fe_3O_4@PC-CDs-Ag NP (Fig. S4B), this result confirms a successful galvanic replacement of the Ag with Au. While the Cu is from the copper grid, the C element can be from both the carbon shell of the hybrid NP and the carbon film coated on the copper grid. The elements of Fe, O, and Au signals should be resulted from the magnetite and Au nanocrystals, respectively. Fig. 2C shows the 2D lattice fringes of Au nanocrystals trapped in the carbon shell. The interplanar distance of about 0.248 nm corresponds well to the (111) lattice planes of Au.[54] Besides the Au nanocrystals, the fluorescent CDs were also found in the carbon shell of the Fe_3O_4@PC-CDs-Au NPs. As demonstrated in Fig. 2E, the interplanar distance of ~0.207 nm of the 2D lattice fringes from the fluorescent CD buried in the carbon shell corresponds to the (104) lattice planes of carbon.[55] The EDAX (Fig. 2F) of the carbon dot further reveals their carbon component while the Cu element results from the copper grid. These data show that a hybrid nanostructure with the Fe_3O_4 nanocrystals clustered in the core and the carbon dots and gold nanocrystals embedded in the carbon shell has been successfully synthesized.

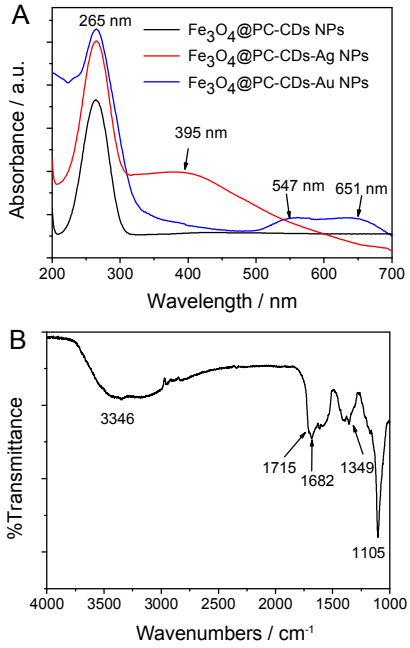

Fig. 3. (A) UV-vis spectra of the Fe_3O_4@PC-CDs, Fe_3O_4@PC-CDs-Ag, and Fe_3O_4@PC-CDs-Au NPs respectively. (B) FT-IR spectrum of the as-obtained Fe_3O_4@PC-CDs-Au NPs.

Fig. 3A shows the typical UV–Visible absorption spectra of the as-obtained Fe_3O_4@PC-CDs NPs, Fe_3O_4@PC-CDs-Ag NPs and Fe_3O_4@PC-CDs-Au NPs, respectively. The Fe_3O_4@PC-CDs template NPs exhibit an absorption peak at 265 nm, which is ascribed to the π-π* transition of aromatic domains in the porous carbon matrix and is similar to that of polycyclic aromatic hydrocarbons.[56,57] The Fe_3O_4@PC-CDs-Ag NPs demonstrate a new peak at about 395 nm, which should be attributed to the

characteristic plasmon resonance bands of isolated spherical Ag nanocrystals embedded in the carbon shell.[58] After the galvanic replacement reaction of the Fe_3O_4@PC-CDs-Ag NPs with $HAuCl_4$, the absorption peak of the Ag nanocrystals disappears. Meanwhile, a new broad absorption peak with a broad absorption range of 500-700 nm can be obviously observed, which indicate that Au nanocrystals in different sizes have been successfully immobilized in the carbon shell of the Fe_3O_4@PC-CDs template NPs.[37] Fig. 3B shows the FT-IR spectrum of the resultant Fe_3O_4@PC-CDs-Au NPs. Compared to the IR spectrum of the precursor Fe_3O_4@PC-CDs-Ag NPs, the absorption bands of –OH and –COOH groups may have a slight shift. However, the peak positions cannot be well defined due to the broad width of –OH peak and shoulder shape of the –COOH peak. Nevertheless, these hydrophilic –COOH and/or –OH groups on the surface of the porous carbon shell explain the excellent stability of the NPs in aqueous phase.

Benefited from the strong fluorescence (Fig. S5A) of the CDs and surface plasma properties of Au nanocrystals, we expect that the Fe_3O_4@PC-CDs-Au NPs should have optical contrasting ability for cell imaging.[39,40,59] In addition, the Fe_3O_4@PC-CDs-Au NPs demonstrate excellent photostability against light irradiation. As shown in Fig. S5B, the PL intensity of the Fe_3O_4@PC-CDs-Au NPs at 457 nm only decreased by ~7.5% after 2 h of continuous exposure to the excitation UV light with λ_{ex} = 365 nm. Here, the mouse melanoma cells B16F10 were selected as model cells to evaluate the cellular imaging function of these Fe_3O_4@PC-CDs-Au NPs. Fig. 4 shows the laser scanning confocal images of the B16F10 cells incubated with the Fe_3O_4@PC-CDs-Au NPs. Similar to the results obtained from the B16F10 cells incubated with the Fe_3O_4@PC-CDs template NPs and Fe_3O_4@PC-CDs-Ag NPs (Fig. S6), these results show that the Fe_3O_4@PC-CDs-Au NPs can also overcome the cellular barriers to enter the intracellular region and light up the cells with strong fluorescence under the excitations of different wavelengths of 405 nm (A), 488 nm (B) and 546 nm (C), respectively. The bright fluorescence in a range of different wavelengths may originate from the synergy of the fluorescent carbon dots and Au nanocrystals embedded in the carbon shells. The Z-scanning confocal fluorescence images of B16F10 cell after incubated with the Fe_3O_4@PC-CDs-Au NPs (Fig. S7) further demonstrate the strong fluorescence in cytoplasm around cell nucleus when excited with a laser of 488 nm. As the complexity of molecular interactions governing the endocytosis are revealed, the mechanisms of endocytosis should be viewed in a broader context than simple vesicular trafficking.[60] Furthermore, the Fe_3O_4@PC-CDs-Au NPs demonstrate excellent photostability as an optical marker. As shown in Fig. 4D-F, the confocal images of the B16F10 cells incubated with the Fe_3O_4@PC-CDs-Au NPs did not show obvious fluorescent intensity change after the prolonged continuous laser irradiation from 0 to 30 min, which provides a possibility for long term cellular imaging application. These results imply that the Fe_3O_4@PC-CDs-Au NPs could be a good candidate as optical marker for fluorescent bioimaging.

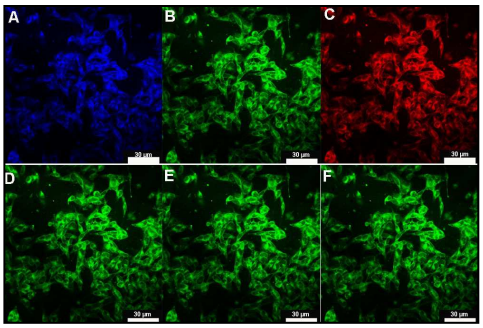

Fig. 4. Laser scanning confocal microscopy images of B16F10 cells incubated with Fe_3O_4@PC-CDs-Au NPs under different excitation wavelengths: (A) 405 nm; (B) 488nm; (C) 546 nm. Laser scanning confocal microscopy images of B16F10 cells incubated with Fe_3O_4@PC-CDs-Au NPs under different excitation time with 488 nm laser: (D) 0 min; (E) 15 min; (F) 30 min.

The porous structure of the carbon shell of the Fe_3O_4@PC-CDs-Au NPs enables the loading of drug molecules. Fig. 5A shows typical N_2 sorption–desorption isotherm of the Fe_3O_4@PC-CDs-Au NPs. The Brunauer–Emmett–Teller (BET) surface area and total pore volume of the Fe_3O_4@PC-CDs-Au NPs determined from the curves are 78.82 m^2 g^{-1} and 0.14 cm^3 g^{-1}, respectively. The average Barrett–Joyner–Halenda (BJH) pore diameters of the Fe_3O_4@PC-CDs-Au NPs calculated from the desorption branch of the isotherm are 6.5 nm and 8.7 nm (Fig. S8). The porous structure with large surface area and carboxyl/hydroxyl surface functional groups of the Fe_3O_4@PC-CDs-Au NPs are highly desirable for drug carrier applications. Here, DOX was selected as a model drug to evaluate the loading capacity of the Fe_3O_4@PC-CDs-Au NPs by simply mixing the NPs with DOX in PBS solution. As shown in the inset of Fig. 5B, after an adequate mixing of the DOX solution with the Fe_3O_4@PC-CDs-Au NPs, an obvious color change of the DOX solution was observed. In addition, the DOX-loaded Fe_3O_4@PC-CDs-Au NPs can be easily separated from the mixture within a few minutes by applying a 0.3 T magnetic field. The much lighter color of the remained DOX solution after removal of the NPs confirms that DOX molecules can be readily loaded into the NPs. By comparing the intensity decrease of the characteristic UV-vis absorption peak of DOX at 480 nm for the initial DOX solution and the remained supernatant DOX solution after removal of DOX-loaded NPs, the amount of DOX loaded into the Fe_3O_4@PC-CDs-Au NPs was determined to be 71.9 wt%. The high drug loading capacity (719 mg/g) of the Fe_3O_4@PC-CDs-Au NPs should be attributed to two factors. First, the DOX molecules can associate with the porous carbon of the Fe_3O_4@PC-CDs-Au NPs through several types of interactions, including the supramolecular π-stacking between the conjugated rings of DOX molecules and the aromatic rings in the carbon shell, the hydrogen bonding between the hydroxyl/amine groups of DOX and the surface hydroxyl/carboxyl groups of the NPs, and the electrostatic attractions between the protonated amine groups of DOX and the dissociated surface carboxylate groups of the Fe_3O_4@PC-CDs-Au NPs.[61,62] Second, the porous structure with lager surface area of the carbon shell of the hybrid NPs provide plenty space for drug storage. Thus, the DOX drug molecules diffusing into the carbon matrix of the Fe_3O_4@PC-CDs-Au NPs can be retained and enriched.

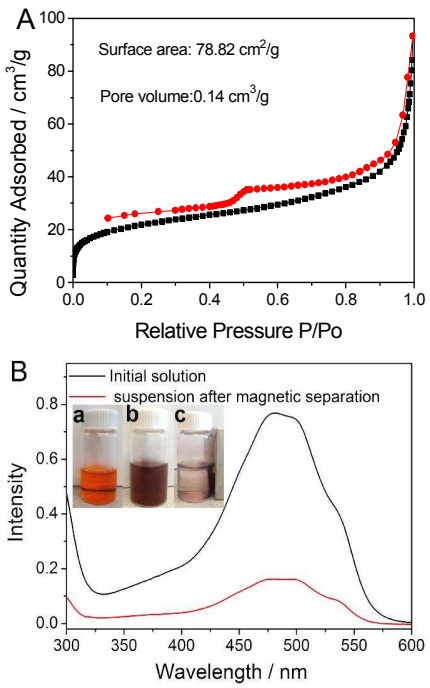

Fig. 5. (A) N_2 adsorption/desorption isotherms of the Fe_3O_4@PC-CDs-Au NPs. (B) UV-vis absorption spectra of the initial DOX solution (0.1 mg/mL) and the supernatant DOX solution after majority of DOX being loaded into the Fe_3O_4@PC-CDs-Au NPs. The inset in (B) is photographs of DOX solution (0.1 mg/mL) in a vial: (a) without addition of Fe_3O_4@PC-CDs-Au NPs; (b) mixed with 1 mg Fe_3O_4@PC-CDs-Au NPs; (c) after removing the Fe_3O_4@PC-CDs-Au NPs from the (b).

The magnetic hysteresis loops of Fe_3O_4@PC-CDs-Au NPs were measured at 300 K in an applied magnetic field of up to 40000 Oe. As shown in Fig. 6A, the Fe_3O_4@PC-CDs NPs exhibited a saturation magnetization of 32.5 emu/g. After the growth of Au nanocrystals on the Fe_3O_4@PC-CDs template NPs, the saturation magnetization of the resulted Fe_3O_4@PC-CDs-Au hybrid NPs is decreased to 23.23 emu/g, which should be attributed to the reduction of the mass content of the magnetic Fe_3O_4 nanocrystals in the Fe_3O_4@PC-CDs-Au NPs. In addition, no hysteretic behavior was observed in the curves, indicating a superparamagnetic state of the Fe_3O_4@PC-CDs-Au NPs. When the aqueous dispersion of the Fe_3O_4@PC-CDs-Au NPs is subjected to a 0.30 T magnetic field, the NPs can be attracted toward the magnet side in a few minutes, as shown in Fig. 6a and b. Slight agitation will bring the hybrid NPs back into the original uniform dispersion in water after the magnetic field was removed (Fig. 6c). The quick magnetic separation and redispersing ability of the newly designed Fe_3O_4@PC-CDs-Au NPs in aqueous phase are desirable for applications in bioseparation, storage, and magnetic targeting drug delivery.

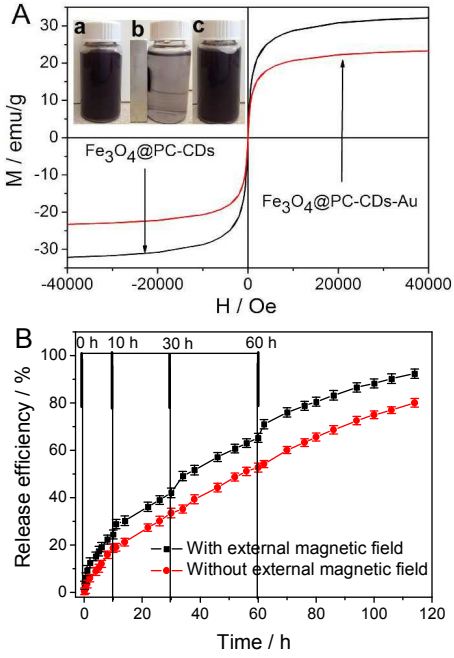

Fig. 6. (A) The hysteresis loops of the Fe_3O_4@PC-CDs template NPs and Fe_3O_4@PC-CDs-Au hybrid NPs measured at room temperature. The inset represents photographs of an aqueous dispersion of the Fe_3O_4@PC-CDs-Au NPs in a vial: (a) without magnetic field, (b) with magnetic field, and (c) after the magnetic field is removed. (B) Releasing profiles of DOX-loaded Fe_3O_4@PC-CDs-Au NPs at a constant temperature of 37 ^{o} C, induced with/without an external alternating magnetic field for 30 min at the cumulative time of 0, 10, 30, and 60 h, respectively.

Considering the high saturation magnetization and superparamagnetic behavior of the Fe_3O_4@PC-CDs-Au NPs, a magnetic-responsive drug releasing behavior from the NPs was examined. For this purpose, the setup for DOX release from the Fe_3O_4@PC-CDs-Au NPs was placed in a magnetic generator inside a thermostatic chamber at 37 ^{o} C, which will realize the heating of the releasing medium containing the NPs by applying an alternating magnetic field. The total amount of released DOX molecules were measured at both the starting point of applying magnetic field and the time point after 30 min continuous exposure to the alternating magnetic field. Fig. 6B shows the release kinetics of DOX from the DOX-loaded Fe_3O_4@PC-CDs-Au NPs immersed in PBS solution of pH = 7.4 at 37 ^{o} C, experiencing an alternating magnetic field at time points of 0, 10, 30, and 60 h, respectively. The release rate of DOX loaded in the Fe_3O_4@PC-CDs-Au NPs shows an obvious enhancement when an alternating magnetic field was applied. When an alternating magnetic field was turned off, the drug release rate returns back to its regular rates similar to the DOX releasing profiles from the NPs without applying external magnetic field. After a cumulative release for 114 h, 92.4% of DOX molecules were released from the DOX-loaded Fe_3O_4@PC-CDs-Au NPs when an alternating magnetic field was applied for 30 min at the releasing stages of 0, 5, 60, and 92 h, respectively. In contrast, only 82% of DOX molecules were release from the NPs during the same time period of 114 h when no external magnetic field was applied. Such an obvious increase in the DOX release rate should be attributed to the local heat produced by the magnetic-thermal conversion (Fig. S9) of the Fe_3O_4@PC-CDs-Au NPs under the alternating magnetic field. The local heat will increase the Brownian motion of DOX molecules and break down some of the interactions between the DOX molecules and the drug hosts of the NPs due to

the enhancement of local temperatures.[63] This mechanism is further confirmed by the temperature-responsive DOX release profiles from the Fe_3O_4@PC-CDs-Au NPs (Fig. S10A), which clearly demonstrated that the increase in temperature from 27 ºC to 37 ºC and 45 ºC can significantly speed up the release of DOX molecules from the Fe_3O_4@PC-CDs-Au NPs. This magnetic responsive release behavior reveals that the newly developed Fe_3O_4@PC-CDs-Au NPs have a potential for on-demand drug delivery system.

Both Fe_3O_4@PC-CDs NPs and Au nanocrystals with strong NIR light absorbing capabilities have been used as photothermal conversion agents for photothermal therapy.[44,47] The growth of the Au nanocrystals onto the Fe_3O_4@PC-CDs template NPs is expected to further enhance the photothermal conversion efficiency of the NIR light. Fig. 7A shows the photothermal effect of water, aqueous dispersion of Fe_3O_4@PC-CDs template NPs (0.1 g L^{-1}), and aqueous dispersion of Fe_3O_4@PC-CDs-Au hybrid NPs (0.1 g L^{-1}) under a NIR irradiation at a power density of 1.5 W/cm^2 for 5 min, respectively. While the water temperature only increases by about 5 °C under the NIR irradiation for 5 min, the temperatures of 0.1 g/L aqueous dispersions of the Fe_3O_4@PC-CDs NPs and Fe_3O_4@PC-CDs-Au hybrid NPs increase by nearly 25 °C and 34 °C, respectively, under the same NIR irradiation for 5 min. Clearly, the Fe_3O_4@PC-CDs template NPs already exhibit very high photothermal conversion ability, while the embedding of Au nanocrystals on the carbon shell can further significantly enhance the photothermal effect of the resultant Fe_3O_4@PC-CDs-Au hybrid NPs. Given this excellent photothermal conversion effect and the porous carbon structure, the Fe_3O_4@PC-CDs-Au hybrid NPs should be an ideal candidate as a new efficient drug carrier for NIR-responsive drug release and photothermal therapy.

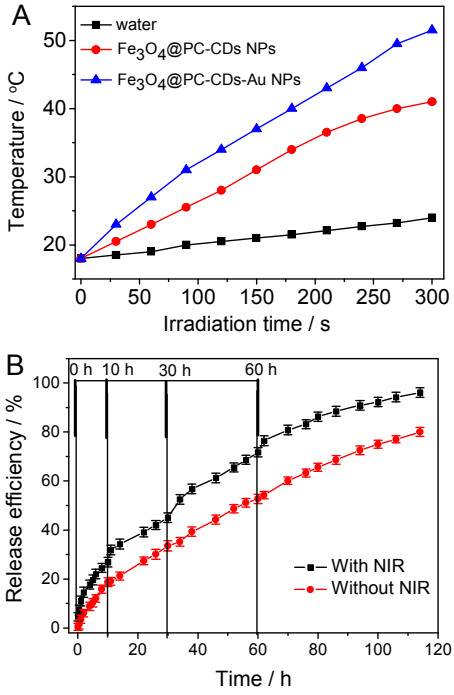

Fig. 7. (A) The photothermal curves of water, aqueous dispersion of Fe_3O_4@PC-CDs NPs (0.1 g L^{-1}), and aqueous dispersion of Fe_3O_4@PC-CDs-Au NPs under a NIR irradiation for 5 min. (B) Releasing profiles of DOX from the Fe_3O_4@PC-CDs-Au NPs at 37 ºC with/without a NIR irradiation of 1.5 W/cm^2 for 5 min at the cumulative time points of 0, 10, 30, and 60 h, respectively.

Fig. 7B compares the DOX release behaviors from the DOX-loaded Fe_3O_4@PC-CDs-Au NPs dispersed in PBS solution at 37 °C, without and with 5 min NIR light irradiation at certain releasing time points, respectively. Without NIR irradiation, only 80.2% of total DOX was released from the NPs after 114 h. In contrast, the 5 min irradiation with NIR light at the releasing stages of 0, 10, 30, and 60 h can obviously speed up the release of DOX molecules from the Fe_3O_4@PC-CDs-Au NPs. During the same releasing period of 114 h, 96.1 % of total DOX could be released from the Fe_3O_4@PC-CDs-Au NPs with the assistance of short time exposure to NIR light. When the NIR light radiation was turned off, the drug release rate returned to its regular slow rate similar to the releasing profiles obtained without the assistance of NIR irradiation. Similar to the alternating magnetic field induced heating effect, the significantly enhanced drug release rate under NIR light irradiation is also attributed to the local heat produced by the efficient photothermal conversion of the Fe_3O_4@PC-CDs-Au NPs, which contain both fluorescent carbon dots and Au nanocrystals. The intensive local heat could not only weaken the drug–host interactions between DOX molecules and the surface carboxyl/hydroxyl groups of porous carbon, but also increase the Brownian motion of DOX molecules at elevated temperatures.[44,47] Besides the heat, the pH can also trigger the drug release rate. As shown in Fig. S10B, the DOX molecules are released at a much faster rate at acidic pH of 5.0 than at pH = 7.4. This acidic pH-triggered fast drug release is beneficial to the cancer treatment because microenvironments of extracellular tissues of tumors are acidic, which can potentially facilitate active drug release from the drug carriers. We expect that the combination of high drug loading capacity and magnetic/NIR dual responsive drug release behavior will provide the new drug carrier of Fe_3O_4@PC-CDs-Au NPs with high therapeutic efficacy.

To further evaluate the potential applications of the Fe_3O_4@PC-CDs-Au NPs as magnetic/NIR-responsive drug carriers, photothermal therapeutic agent, and bioimaging contrasting agent, an in vitro cytotoxicity study of the hybrid NPs under different conditions were elaborately conducted against B16F10 cells. Fig. 8A compares the in vitro cytotoxicity of the drug-free and DOX-loaded Fe_3O_4@PC-CDs-Au NPs without/with the assistance of 1.5 W/cm^2 NIR irradiation for 5 min after incubated for 24 h in the concentration range of 25 μg/mL to 100 μg/mL. Clearly, without the 5 min NIR irradiation, the drug-free Fe_3O_4@PC-CDs-Au NPs have no harm to the cells, indicating the non- or low cytotoxicity of the Fe_3O_4@PC-CDs-Au NPs. In contrast, the introduction of 5-min NIR irradiation in the presence of the drug-free Fe_3O_4@PC-CDs-Au NPs can significantly enhance the cytotoxicity. For example, 32-48% of tumor cells could be killed by the 5 min NIR irradiation in the presence of 25-100 μg/mL Fe_3O_4@PC-CDs-Au hybrid NPs. However, the control experiment with the 5 min NIR irradiation treatment alone has little influence on the cytotoxicity (Fig. S11), which indicates that the photothermal effect can only be observed in the presence of Fe_3O_4@PC-CDs-Au NPs. This result implies that the newly developed Fe_3O_4@PC-CDs-Au NPs can be used as an efficient photothermal agent to kill tumor cells under NIR irradiation. Without the assistance of 5-min NIR irradiation, the DOX-loaded Fe_3O_4@PC-CDs-Au NPs could kill about 12-33% cancer cells in 24 h as the concentration increased from 25 to 100 μg/mL, which is understandable because only about 27.4% of the loaded DOX can be released in the first 24 h (Fig. 7B). In contrast, the addition of 5-min NIR irradiation in combined with the DOX-loaded Fe_3O_4@PC-CDs-Au NPs in the same concentration range of 25-100 μg/mL could kill about 67-88% cancer cells. This significantly enhanced cytotoxicity of the

DOX-loaded Fe_3O_4@PC-CDs-Au NPs in combination with 5-min NIR irradiation is even higher than the simple additive results from the independent NIR photothermal treatment and the DOX chemo treatment, which indicate that the developed Fe_3O_4@PC-CDs-Au NPs could produce a synergistic effect from the combined chemo-/photothermal treatment to provide excellent therapeutic efficacy.

Considering that the Fe_3O_4@PC-CDs-Au NPs are synthesized based on the Fe_3O_4@PC-CDs NPs and Fe_3O_4@PC-CDs-Ag NPs, we also compare the in vitro cytotoxicity of the Fe_3O_4@PC-CDs NPs, Fe_3O_4@PC-CDs-Ag NPs, and Fe_3O_4@PC-CDs-Au NPs in the absence and presence of 1.5 W/cm^2 NIR irradiation for 5 min. As shown in Fig. 8B, without the assistance of 5 min NIR irradiation, all the three types of hybrid NPs have no harm to the cells in the concentration range of 25-100 μg/mL. After introducing the 5 min NIR irradiation, the cytotoxicity with the Fe_3O_4@PC-CDs-Ag NPs as photothermal therapeutic agent is nearly the same as the cytotoxicity with the Fe_3O_4@PC-CDs as photothermal agent. This result indicates that the addition of Ag nanocrystals onto the Fe_3O_4@PC-CDs does not increase the NIR photothermal effect, which is understandable because Ag nanocrystals do not absorb NIR photons. The photothermal effects of both Fe_3O_4@PC-CDs and Fe_3O_4@PC-CDs-Ag NPs are contributed by the carbon dots embedded in the carbon shell of the NPs. In contrast, the 5 min NIR irradiation with the Fe_3O_4@PC-CDs-Au NPs as photothermal therapeutic agent demonstrate much higher efficacy to kill the tumor cells in comparison with the Fe_3O_4@PC-CDs and Fe_3O_4@PC-CDs-Ag NPs as therapeutic agents. This result clearly proves that the addition of Au nanocrystals onto the Fe_3O_4@PC-CDs NPs has a great advantage to further improve the photothermal conversion ability and the Fe_3O_4@PC-CDs-Au NPs can serve as a highly efficient photothermal therapeutic agent for cancer treatment.

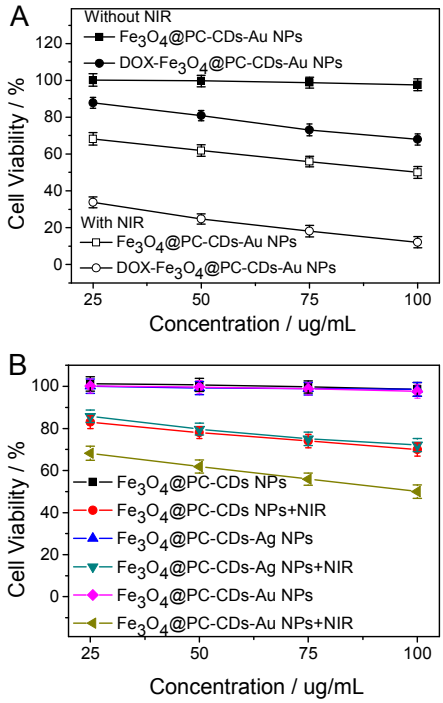

Fig. 8. (A) In vitro cytotoxicity of drug-free and DOX-loaded Fe_3O_4@PC-CDs-Au NPs with/without 5 min exposure to the 1.5 W/cm^2 NIR light, respectively. (B) In vitro cytotoxicity of Fe_3O_4@PC-CDs template NPs, Fe_3O_4@PC-CDs-Ag NPs, and Fe_3O_4@PC-CDs-Au NPs with and without 5-min exposure to NIR light, respectively.

4. Conclusions

In summary, a multifunctional hybrid NPs that can integrate the magnetic Fe_3O_4 nanocrystals, fluorescent carbon dots, and Au nanocrystals into a porous carbon matrix can be successfully synthesized by first preparation of core-shell structured Fe_3O_4@PC-CDs template NPs, followed by loading and in-situ reduction of Ag^+ ions and a final replacement of Ag with Au nanocrystals through a galvanic reaction. The resultant Fe_3O_4@PC-CDs-Au hybrid NPs can combine the material properties from each component to provide a multifunctional nanoplatform. The NPs can overcome cellular barriers to enter into the intracellular region and light up the mouse melanoma B16F10 cells under the excitation of laser benefited from the stable and strong fluorescence of carbon dots. The NPs can be easily dispersed into water and carry drug molecules with a high loading capacity benefited from the porous carbon structure and hydrophilic hydroxyl/carboxyl surface functional groups. The NPs can be easily guided by an external magnetic field benefited from the superparamagnetic nature and high saturation magnetization of the magnetite nanocrystals clustered in the core, which also produce a localized heat to trigger the release of the loaded drug under an alternating magnetic field. Benefited from the combined photothermal effects of carbon dots and Au nanocrystals embedded in the carbon matrix, the NPs cannot only serve as highly efficient NIR photothermal therapeutic agents to kill cancer cells, but also regulate the release rate of the loaded drug under the NIR irradiation. The NPs can produce a synergistic effect from the combined chemo-/photothermal treatment to provide high therapeutic efficacy. Such designed multifunctional nanoplatform with fluorescent imaging ability, magnetic/NIR-responsive drug delivery, and high photothermal therapeutic ability have great potential for various biomedical applications.

Acknowledgements

We gratefully acknowledge the financial support from the American Diabetes Association (Basic Science Award 1-12-BS-243) and PSC-CUNY Research Award (66076-00 44). A portion of this research was conducted at the Center for Nanophase Materials Sciences, which is sponsored at Oak Ridge National Laboratory by the Scientific User Facilities Division, Office of Basic Energy Sciences, U.S. Department of Energy.

Notes and references

[a] *Department of Chemistry, The College of Staten Island, and The Graduate Center, The City University of New York, Staten Island, NY 10314 USA. E-mail address: shuiqin.zhou@csi.cuny.edu; Tel.: +1 718 982 3897; Fax: +1 718 982 3910. A*

[b] *Center for Nanophase Materials Sciences and Chemical Science Division, Oak Ridge National Laboratory, Oak Ridge, TN 37831, USA*

† Electronic Supplementary Information (ESI) available: Fig. S1-Fig. S11. See DOI: 10.1039/b000000x/

References

1 S. N. Baker and G. A. Baker, *Angew. Chem., Int. Ed.*, 2010, **49**, 6726.
2 P. G. Luo, S. Sahu, S. T. Yang, S. K. Sonkar, J. Wang, H. Wang, G. E. LeCroy , L. Cao and Y. P. Sun, *J. Mater. Chem. B,* 2013, **1**, 2116.
3 B. Hu, K. Wang, L. Wu, S. Yu, M. Antonietti and M. Titirici, *Adv. Mater.,* 2010, **22**, 813.
4 Z. M. Markovic, L. M. Harhaji-Trajkovic, B. M. Todorovic-Markovic, D. P. Kepić, K. M. Arsikin, S. P. Jovanović, A. C. Pantovic, M. D. Dramićanin and V. S. Trajkovic, *Biomaterials,* 2011, **32**, 1121.
5 Q. Liu, L. Cui and D. Losic, *Acta. Biomater.,* 2013, **9**, 9243.
6 H. Huang, E. Pierstorff, E. Osawa and D. Ho, *Nano Lett.,* 2007, **7**, 3305.
7 Z. Liu, X. Sun, N. Nakayama-Ratchford and H. Dai, *ACS Nano,* 2007, **1**, 50.

8 Q. Wang, X. Huang, Y. Long, X. Wang, H. Zhang, R. Zhu, L. Liang, P. Teng and H. Zheng, *Carbon,* 2013, **59**, 192.
9 J. Gu, S. Su, Y. Li, Q. He and J. Shi, *Chem. Commun.,* 2011, **47**, 2101.
10 A. Montellano, T. Da Ros, A. Bianco and M. Prato, *Nanoscale,* 2011, **3**, 4035.
11 G. Gollavelli and Y. Ling, *Biomaterials,* 2014, **35**, 4499.
12 C. Wang, S. Ravi, S. Garapati, M. Das, M. Howell, J. Mallela, S. Alwarappan, S. Mohapatra and S. Mohapatra, *J. Mater. Chem. B,* 2013, **1**, 4396.
13 C. Stefanadis, C. Chrysochoou, D. Markou, K. Petraki, D. B. Panagiotakos, C. Fasoulakis, A. Kyriakidis, C. Papadimitriou and P. K. Toutouzas, *J. Clin. Oncol.,* 2001, **19**, 676.
14 I. F. Tannock and D. Rotin, *Cancer Res.,* 1989, **49**, 4373.
15 C. Song, V. Appleyard, K. Murray, T. Frank, W. Sibbett, A. Cuschieri and A. Thompson, *Int. J. Cancer,* 2007, **121**, 1055.
16 S. M. Lee, H. Park and K. H. Yoo, *Adv. Mater.,* 2010, **22**, 4049.
17 H. Wang, A. Mararenko, G. Cao, Z. Gai, K. Hong, P. Banerjee and S. Zhou, *ACS Appl. Mater. Interfaces,* 2014, **6**, 15309.
18 J. Chen, Z. Guo, H. Wang, M. Gong, X. Kong, P. Xia and Q. Chen, *Biomaterials,* 2013, 34, 571.
19 F. Yang, D. L. Fu, J. Long and Q. X. Ni, *Med. Hypotheses*, 2008, **4**, 765.
20 H. Wang, J. Yi, S. Mukherjee, P. Banerjee and S. Zhou, *Nanoscale,* 2014, **6**, 13001.
21 G. Mikhaylov, U. Mikac, A. Magaeva, V. I. Itin, E. P. Naiden, I. Psakhye, L. Babes, T. Reinheckel, C. Peters, R. Zeiser, M. Bogyo, V. Turk, S. G. Psakhye, B. Turk and O. Vasiljeva, *Nat. Nanotechnol.,* 2011, **6**, 594.
22 P. Guardia, R. D. Corato, L. Lartigue, C. Wilhelm, A. Espinosa, M. Garcia-Hernandez, F. Gazeau, L. Manna and T. Pellegrino, *ACS Nano,* 2012, **6**, 3080.
23 C. Martinez-Boubeta, K. Simeonidis, D. Serantes, I. Conde-Leboran, I. Kazakis, G. Stefanou, L. Pena, R. Galceran, L. Balcells, C. Monty, D. Baldomir, M. Mitrakas and M. Angelakeris, *Adv. Funct. Mater.,* 2012, **22**, 3737.
24 Y. Krupskaya, C. Mahn, A. Parameswaran, A. Taylor, K. Krämer, S. Hampel, A. Leonhardt, M. Ritschel, B. Büchner and R. Klingeler, *J. Magn. Magn. Mater.,* 2009, **321**, 4067.
25 F. F. Jöbsisvander-Vleit, *J. Biomed. Opt.,* 1999, **4**, 392.
26 M. Ferrari and V. Quaresima, *Neuroimage,* 2012, **63**, 921.
27 H. Wang, J. Shen, G. Cao, Z. Gai, K. Hong, P. R. Debata, P. Banerjee and S. Zhou, *J. Mater. Chem. B,* 2013, **1**, 6225.
28 H. Wang, F. Ke, A. Mararenko, Z. Wei, P. Banerjee and S. Zhou, *Nanoscale,* 2014, **6**, 7443.
29 N. Li, Z. Yu, W. Pan, Y. Han, T. Zhang and B. Tang, *Adv. Funct. Mater.,* 2013, **23**, 2255.
30 R. Chen, X. Zheng, H. Qian, X. Wang, J. Wang and X. Jiang, *Biomater. Sci.,* 2013, **1**, 285.
31 Y. Chien, Y. Chou, S. Wang, S. Hung, M. Liau, Y. Chao, C. Su, C. Yeh, *ACS Nano,* 2013, **7**, 8516.
32 M. S. Yavuz, Y. Cheng, J. Chen, C. M. Cobley, Q. Zhang, M. Rycenga, J. Xie, C. Kim, K. H. Song, A. G. Schwartz, L. V. Wang and Y. Xia, *Nat. Mater.,* 2009, **8**, 935.
33 M. Prato, K. Kostarelos and A. Bianco, *Acc. Chem. Res.,* 2008, **41**, 60.
34 S. Pandey, M. Thakur, A. Mewada, D. Anjarlekar, N. Mishra and M. Sharon, *J. Mater. Chem. B,* 2013, **1**, 4972.
35 Z. Cheng, R. Chai, P. Ma, Y. Dai, X. Kang, H. Lian, Z. Hou, C. Li and J. Lin, *Langmuir,* 2013, **29**, 9573.
36 L. Wang, J. Shi, X. Jia, R. Liu, H. Wang, Z. Wang, L. Li, J. Zhang, C. Zhang and Z. Zhang, *Pharm. Res.*, 2013, **30**, 2757.
37 Y. Zhou, H. Wang, M. Gong, Z. Sun, K. Cheng, X. Kong, Z. Guo and Q. Chen, *Dalton Trans.,* 2013, **42**, 9906.
38 S. Prakash, M. Malhotra, W. Shao, C. Tomaro-Duchesneau and S. Abbasi, *Adv. Drug Deliv. Rev.,* 2011, **63**, 1340.
39 M. Ravera, G. Bagni, M. Mascini, J. C. Dabrowiak and D. Osella, *J. Inorg. Biochem.,* 2007, **101**, 1023.
40 Y. Kawai, T. Nakao, N. Kunimura, Y. Kohda and M. Gemba, *J. Pharmacol. Sci.,* 2006, **100**, 65.
41 S. M. Lee, H. Park and K. H. Yoo, *Adv. Mater.,* 2010, **22**, 4049.
42 A. M. Alkilany, L. B. Thompson, S. P. Boulos, P. N. Sisco and C. J. Murphy, *Adv. Drug Delivery Rev.,* 2012, **64**, 190.
43 X. H. Huang, I. H. El-Sayed, W. Qian and M. A. El-Sayed, *J. Am. Chem. Soc.,* 2006, **128**, 2115.
44 S. E. Skrabalak, J. Chen, Y. Sun, X. Lu, L. Au, C. M. Cobley and Y. Xia, *Acc. Chem. Res.,* 2008, **41**, 1587.
45 T. B. Huff, L. Tong, Y. Zhao, M. N. Hansen, J. X. Cheng and A. Wei, *Nanomedicine,* 2007, **2**, 125.
46 C. J. Liu, C. H. Wang, C. C. Chien, H. T. Chen, T. E. Hua, W. H. Leng, H. H. Chen, I. M. Kempson, Y. Hwu, M. Hsiao, T. C. Lai, J. L. Wang, C. S. Yang, H. M. Lin, Y. J. Chen and G. Margaritondo, *Mater. Chem. Phys.,* 2011, **126**, 352.
47 H. Wang, J. Sheng, Y. Li, Z. Wei, G. Cao, Z. Gai, K. Hong, P. Banerjee and S. Zhou, *Biomater. Sci.,* 2014, **2**, 915.
48 W. Wu, T. Zhou and S. Zhou, *Chem. Mater.,* 2009, **21**, 2851.
49 L. Au, X. M. Lu and Y. N. Xia, *Adv. Mater.,* 2008, **20**, 2517
50 H. Wang, Q. W. Chen, Y. F. Yu, K. Cheng and Y. B. Sun, *J. Phys. Chem. C,* 2011, **115**, 11427.
51 G. Socrates, Infrared and Raman characteristic group frequencies: Tables and Charts, 3rd ed; John Wiley& Sons Ltd: Chichester, 2001.
52 Coates, Interpretation of Infrared Spectra, A Practical Approach. In "*Encyclopedia of Analytical Chemistry*", Meyers, R. A. Ed., John Wiley & Sons Ltd, Chichester, **2000**, pp10815-10837.
53. Y. Sun and Y. Wang. *Nano Lett.,* 2011, **11**, 4386.
54 H. Yu, M. Chen, P. M. Rice, S. X. Wang, R. L. White and S. Sun, *Nano Lett.,* 2005, **5**, 379.
55 L. Tian, D. Ghosh, W. Chen, S. Pradhan, X. Chang and S. Chen, *Chem. Mater.,* 2009, **21**, 2803.
56 S. J. Yu, M. W. Kang, H. C. Chang, K. M. Chen and Y. C. Yu. *J. Am. Chem. Soc.,* 2005, **127**, 17604.
57 Y. R. Chang, H. Y. Lee, K. Chen, C. C. Chang, D. S. Tsai, C. C. Fu, T. S. Lim, Y. K. Tzeng, C. Y. Fang, C. C. Han, H. Chang and W. Fan, *Nat. Nanotechnol.,* 2008, **3**, 284.
58 Q. Zhang, W. Y. Li, C. Moran, J. Zeng, J. Y. Chen, L. P. Wen and Y. Xia, *J. Am. Chem. Soc.,* 2010, **132**, 11372.
59 L. Cao, X. Wang, M. Meziani, F. Lu, H. Wang, P. Luo, Y. Lin, B. Harruff, L. Veca, D. Murray, S. Xie and Y. Sun, *J. Am. Chem. Soc.,* 2007, **129**, 11318.
60 S. D. Conner and S. L. Schmld, *Nature,* 2003, **422**, 37.
61 X. Sun, Z. Liu, K. Welsher, J. T. Robinson, A. Goodwin, S. Zaric and H. Dai, *Nano Res.,* 2008, **1**, 203.
62 M. Ma, H. Chen, Y. Chen, X. Wang, F. Chen, X. Cui and J. Shi, *Biomaterials,* 2012, **33**, 989.
63 L. Chen, L. Li, H. Zhang, W. Liu, Y. Yang, X. Liu and B. Xu, *RSC Adv.,* 2014, **4**, 46806.